

# Comparison of Various Voltage Metrics for the Evaluation of the Nonradiative Voltage Loss in Quantum-Structure Solar Cells

Meita Asami<sup>1</sup>, Kentaroh Watanabe, *Member, IEEE*, Riko Yokota, Yoshiaki Nakano, and Masakazu Sugiyama

**Abstract**—There are several methods for the evaluation of the performance of solar cells through the voltage loss. However, the advantages and disadvantages of each method have not been thoroughly discussed nor elucidated. This study compares these various methods to clarify their advantages and disadvantages. The bandgap offset  $W_{OC}$  has been used for the evaluation of the voltage loss. However, it was found that such approach gives inaccurate assessment of the voltage loss in thin-bulk and quantum-structure solar cells. Our study discusses the reasons for such inaccuracy and proves that we can accurately evaluate the nonradiative voltage loss in quantum-structure solar cells using the optoelectronic reciprocity theorem and detailed-balance theory. Our findings enable a fair, accurate, and accessible evaluation of the nonradiative voltage loss in solar cells which facilitates the development of high-efficiency quantum-structure solar cell.

**Index Terms**—Bandgap-voltage offset, electroluminescence (EL), III–V semiconductor material, photovoltaic cell, quantum structure, quantum well, reciprocity relation.

## I. INTRODUCTION

HIGH-PERFORMANCE solar cells exhibit low nonradiative recombination energy loss and they efficiently utilize the energy of photo-generated carriers as electrical energy; however, crystal defects induce nonradiative recombination causing the energy of the photo-generated carriers in solar cells to be lost as thermal energy [1], [2]. High-performance solar cells, which can achieve high energy conversion efficiency and generate large amounts of electricity in limited areas, are needed to realize eco-friendly automobiles [3].

Manuscript received 16 August 2022; revised 3 November 2022; accepted 6 December 2022. Date of publication 30 December 2022; date of current version 12 January 2023. This work was supported in part by New Energy and Industrial Technology Development Organization under Grant JPNP20015 and in part by the Grant-in-Aid for JSPS Research Fellow under Grant JP22J14682. (Corresponding author: Meita Asami.)

Meita Asami, Riko Yokota, and Yoshiaki Nakano are with the Department of Electrical Engineering and Information Systems, School of Engineering, The University of Tokyo, Tokyo 113–8654, Japan (e-mail: asami@hotaka.t.u-tokyo.ac.jp; yokota@enesys.rcast.u-tokyo.ac.jp; nakano@ee.t.u-tokyo.ac.jp).

Kentaroh Watanabe and Masakazu Sugiyama are with the Research Center for Advanced Science and Technology, The University of Tokyo, Tokyo 153–8904, Japan (e-mail: kentaro-h.watanabe@g.ecc.u-tokyo.ac.jp; sugiyama@ee.t.u-tokyo.ac.jp).

Color versions of one or more figures in this article are available at <https://doi.org/10.1109/JPHOTOV.2022.3229186>.

Digital Object Identifier 10.1109/JPHOTOV.2022.3229186

To facilitate high energy conversion efficiency in solar cells, an accurate and accessible evaluation method of voltage loss in solar cells is indispensable. There are several methods for the evaluation of voltage loss. However, the advantages and disadvantages of each method have not been thoroughly discussed nor elucidated. To accurately evaluate the voltage loss in solar cells, we must select the appropriate method.

Bandgap offset  $W_{OC}$  is a widely used voltage metric for the evaluation of the quality of solar cells [4].  $W_{OC}$  is expressed as follows:

$$W_{OC} = E_g/q - V_{OC} \quad (1)$$

where  $V_{OC}$  is the open-circuit voltage,  $E_g$  is the bandgap, and  $q$  is the elementary charge.  $W_{OC}$  indicates the quality of solar cells in the form of an open-circuit voltage loss. In general, a solar cell that has a  $W_{OC}$  lower than 0.4 V is considered to be a high-quality solar cell [4].  $W_{OC}$  is convenient for comparing the voltage loss in solar cells having different bandgaps because it can be calculated easily using (1). Thus, the voltage loss in various types of solar cells, including quantum-structure solar cells, has been evaluated using  $W_{OC}$  [5], [6], [7], [8], [9]. However, in 2018, Ekins-Daukes and Pusch [10] pointed out that  $W_{OC}$  gives a highly optimistic measure of the voltage loss when it is applied to quantum-structure solar cells.  $W_{OC}$  is strongly dependent on the external quantum efficiency (EQE) profile. They found that low EQE at the band-edge of quantum-structure solar cells resulted in a highly optimistic value of  $W_{OC}$ . It was reported that a quantum dot solar cell showed an unphysically low  $W_{OC}$  of 0.04 V [10].

We discuss the pros and cons of each method for the evaluation of the voltage loss in quantum-structure solar cells. This discussion is applicable to not only quantum-structure solar cells but also Si, III–V compound semiconductor, perovskite, and chalcopyrite solar cells. Our study theoretically proved that the voltage metric based on detailed-balance theory, which is denoted as  $W_{DB}$  in (2), is suitable and accessible for the accurate evaluation and fair comparison of the nonradiative voltage loss in quantum-structure solar cells. We experimentally demonstrated the advantage of using  $W_{DB}$  as an indicator of the nonradiative voltage loss in quantum-structure solar cells by fabricating and characterizing two different types of quantum-structure solar cells.

## II. VOLTAGE METRICS

In this section, we introduce the voltage metrics for the evaluation of solar cells used in this article.

### A. $W_{OC}$ and $W_{DB}$

$W_{OC}$  and  $W_{DB}$  are the voltage metrics for analyzing the voltage loss in solar cells. As mentioned in the previous section,  $W_{OC}$  is expressed as (1), and  $W_{DB}$  is expressed as follows:

$$W_{DB} = V_{OC}^{DB} - V_{OC} \quad (2)$$

where  $V_{OC}^{DB}$  is the open-circuit voltage derived from detailed-balance theory [11].  $V_{OC}^{DB}$  is expressed as in the following equations:

$$J(V) = J_{SC} - J_{em,0} (\exp(qV/kT) - 1)$$

$$\begin{aligned} J(V_{OC}^{DB}) = 0 &= J_{SC} - J_{em,0} (\exp(qV_{OC}^{DB}/kT) - 1) \\ &\approx J_{SC} - J_{em,0} \exp(qV_{OC}^{DB}/kT) \\ &\because \exp(qV_{OC}^{DB}/kT) \gg 1 \end{aligned}$$

$$V_{OC}^{DB} = \frac{kT}{q} \ln \left( \frac{J_{SC}}{J_{em,0}} \right) \quad (3)$$

$$J_{SC} = q \int_0^\infty Q_e \phi_{sun} dE \quad (4)$$

$$J_{em,0} = q \int_0^\infty Q_e \phi_{bb} dE \quad (5)$$

where  $J$  is the current density,  $V$  is the voltage,  $J_{SC}$  is the short-circuit current density,  $J_{em,0}$  is the diode saturation current,  $k$  is the Boltzmann constant,  $T$  is the temperature,  $E$  is the energy,  $Q_e$  is the EQE of the solar cell,  $\phi_{sun}$  is the solar irradiance flux, and  $\phi_{bb}$  is the black body radiation flux. The upper limit of the integrals in (4) and (5) is usually set to  $\infty$ . However, in a real situation, we can set the upper limit at a certain energy level such as 4.133 eV (300 nm) because the AM1.5G solar irradiance flux  $\phi_{sun}(\lambda)$  and black body radiation flux  $\phi_{bb}(\lambda)$  at room temperature are negligibly small for  $\lambda \leq 300$  nm; for example,  $\frac{\phi_{sun}(300 \text{ nm})}{\phi_{sun}(700 \text{ nm})} = 3.4 \times 10^{-4}$ ,  $\frac{\phi_{bb}(300 \text{ nm})}{\phi_{bb}(700 \text{ nm})} = 3.4 \times 10^{-39}$ . Therefore, in this study, we measure the EQE in the range of 300–1100 nm, and set the upper limit of the integrals to 4.133 eV (300 nm).

$W_{OC}$  takes  $E_g/q$  as a reference value for the open-circuit voltage, and  $W_{DB}$  takes  $V_{OC}^{DB}$  as a reference value. A smaller value of  $W_{OC}$  or  $W_{DB}$  indicates that the open-circuit voltage of a solar cell is closer to its reference open-circuit voltage, and the voltage loss is lower.

In the solar cell community, including the quantum-structure solar cell community, the bandgap is usually determined by luminescence measurements. The energy of the strongest luminescence peak position is taken as the effective bandgap  $E_{g, lum}$  of the entire solar cell. The energy of quasi-Fermi splitting  $E_{split}^{qfl}(V_{OC})$  does not exceed the bandgap of the solar cell. Since the following equation holds for solar cells, including quantum-structure solar cells,  $W_{OC}$  takes  $E_g/q$  as a reference

voltage.

$$E_{g, lum} > E_{split}^{qfl}(V_{OC}) \approx qV_{OC}. \quad (6)$$

However, a preceding study had pointed out that  $E_{g, lum}/q$  is not a reliable reference voltage for some quantum-structure solar cells;  $W_{OC}$  becomes unphysically low if we use this reference voltage for the calculation of  $W_{OC}$  [10]. To solve this problem, Sayed et al. [12] applied the “detailed-balance-equivalent” method to quantum-structure solar cells to determine the effective bandgap  $E_{g,0}$ . As a reference, we briefly explain the method to calculate  $E_{g,0}$ . Steiner et al. [13] and Geisz et al. [14] posited the step-function EQE, which was unity above  $E_{g,0}$  and zero below  $E_{g,0}$ ; using (5), the saturation current  $J_{em,0}^{step}$  was calculated as follows:

$$\begin{aligned} J_{em,0}^{step} &= q \int_0^\infty Q_e \phi_{bb} dE = q \int_{E_{g,0}}^\infty \phi_{bb} dE \\ &= \frac{2\pi q(kT)^3}{h^3 c^2} \left[ \left( \frac{E_{g,0}}{kT} \right)^2 + 2 \frac{E_{g,0}}{kT} + 2 \right] e^{-\frac{E_{g,0}}{kT}}. \end{aligned} \quad (7)$$

$E_{g,0}$  is numerically calculated under the condition  $J_{em,0}^{step} = J_{em,0}$ .  $J_{em,0}$  is calculated using measured EQE and (5). Thus,  $E_{g,0}$  is the effective absorption edge of a solar cell, which yields  $J_{em,0}$  under the assumption of unit-step EQE. To clarify the calculation method for  $W_{OC}$ , we have used  $W_{OC}^{lum}$  and  $W_{OC}^{eqe}$  in this article.  $W_{OC}^{lum}$  and  $W_{OC}^{eqe}$  use  $E_{g, lum}$  and  $E_{g,0}$  as effective bandgaps, respectively.

There are other methods to determine the bandgap of solar cells using the EQE; however, we found that these methods could not be applied to quantum-structure solar cells because of the distinctive shape of the EQE caused by the excitonic peak (cf. Appendix A). Thus, in this study, we used only  $E_{g, lum}$  and  $E_{g,0}$  as effective bandgaps for the calculation of  $W_{OC}$ .

### B. Advantage of $W_{DB}$ and $W_{OC}^{eqe}$ Over $W_{OC}^{lum}$

The purpose of this section is to compare three voltage metrics:  $W_{OC}^{lum}$ ,  $W_{OC}^{eqe}$ , and  $W_{DB}$ . To make the calculation simple and intuitively understandable, we made four assumptions, which constitute only an example; however, we have tried to reproduce the actual quantum-structure solar cells as much as possible while keeping simplicity. To elucidate the advantage of  $W_{DB}$  and  $W_{OC}^{eqe}$  and the disadvantage of  $W_{OC}^{lum}$ , taking  $E_{g, lum}/q$  as a reference voltage, we performed the simulation with the four assumptions listed in the following.

*Assumption 1:* Double-step-function EQE model

We assumed the EQE profiles shown in Fig. 1 and expressed in the following equation:

$$\begin{aligned} EQE(\lambda) &= \begin{cases} 1 & (300 \text{ nm} \leq \lambda \leq 800 \text{ nm}) \\ 0 \leq EQE_{800-900 \text{ nm}} \leq 1 & (800 \text{ nm} \leq \lambda \leq 900 \text{ nm}) \\ 0 & (\lambda \geq 900 \text{ nm}) \end{cases} \end{aligned} \quad (8)$$

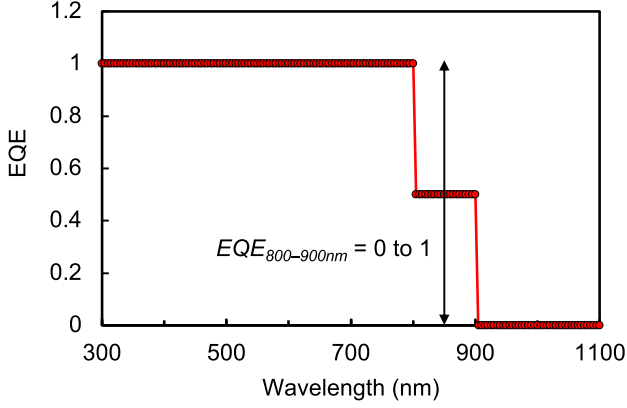


Fig. 1. Double-step-function EQE model. This EQE profile is defined in (8) and plotted at 5 nm intervals.

This double-step-function EQE model was also used in [10].  $EQE_{800-900nm}$  changed from 0 to 1 in the simulation. When we change the thickness of the quantum-structure-active-absorption layer, the longer-wavelength region of EQE changes considerably. Thus, in the double-step-function EQE model, we changed the EQE at near-absorption-edge denoted as  $EQE_{800-900nm}$ . The increase in the EQE at near-absorption-edge corresponds to the increase in the thickness of the quantum-structure-active-absorption layer.

#### Assumption 2: PL peak position

In general, the thickness of the quantum-structure layer does not affect the strongest PL peak position, even if the layer is thin. Photo-excited carriers are confined in quantum wells and radiatively recombined. Here, we assume the strongest PL peak position of the solar cell to be 1.459 eV (850 nm). Thus, the bandgap  $E_{g,lum}$  of the solar cell is also assumed to be 1.459 eV.

#### Assumption 3: Nonradiative recombination current

A preceding study examined the advantage of  $W_{DB}$  over  $W_{OC}$  [11], but in the calculation model based on detailed-balance theory, only the radiative recombination current  $J_{em,0}(\exp(qV/kT) - 1)$  was taken into consideration. In the detailed-balance theory, the external radiative efficiency (ERE) is assumed to be 100%, and the nonradiative recombination current is assumed to be zero. To take the nonradiative recombination into consideration, we added the term  $J_{nr}(V)$  to the basic diode equation. We defined the diode characteristics as follows:

$$J_{dark}(V) = J_{em,0}(\exp(qV/kT) - 1) + J_{nr}(V) \quad (9)$$

where  $J_{nr}(V)$  is the nonradiative current.

To calculate the J–V characteristics of diodes with nonradiative recombination current, we considered  $J_{nr}(V)$ . When the current is injected into a solar cell, it works as a light-emitting diode (LED) and emits electroluminescence (EL). A solar cell under dark condition can be characterized by the ERE of the LED, which is denoted as  $\eta_{ext}(V)$ .  $J_{nr}(V)$  can be defined using the ERE because the ERE is expressed using the following

equation [15].

$$\begin{aligned} \eta_{ext}(V) &= \frac{J_{em,0}(\exp(qV/kT) - 1)}{J_{dark}(V)} \\ &= \frac{J_{em,0}(\exp(qV/kT) - 1)}{J_{em,0}(\exp(qV/kT) - 1) + J_{nr}(V)} \\ &\approx \frac{J_{em,0} \exp(qV/kT)}{J_{em,0} \exp(qV/kT) + J_{nr}(V)} \end{aligned} \quad (10)$$

$$\begin{aligned} \therefore J_{nr}(V) &= (1 - \eta_{ext}(V)) J_{dark}(V) \\ &= \frac{1 - \eta_{ext}(V)}{\eta_{ext}(V)} J_{em,0} \exp(qV/kT) \end{aligned} \quad (11)$$

$\eta_{ext}(V)$  represents the ratio of the radiative recombination current to the injected current  $J_{inj}$ .  $\eta_{ext}(V)$  can also be expressed as follows:

$$\eta_{ext}(V) = \frac{J_{em,0} \exp(qV/kT)}{J_{em,0} \exp(qV/kT) + J_{nr}(V)} = \frac{q\Phi_{abs}}{J_{inj}} \quad (12)$$

where  $\Phi_{abs}$  is the absolute EL flux.  $\eta_{ext}$  is usually calculated using the absolute EL measurement results. The ERE shows the ratio between the injected and radiatively recombined carriers. A solar cell having low ERE has a large nonradiative recombination energy loss. We assume the ERE at the open-circuit voltage to be 1%, which is similar to the ERE of our fabricated samples shown later in this study.

$$\eta_{ext}(V_{OC}) = 0.01 = 1\%.$$

#### Assumption 4: Superposition principle

The J–V characteristic of a solar cell can be written as follows:

$$J(V) = J_{ph}(V) - J_{dark}(V) \quad (13)$$

where  $J_{ph}(V)$  is the photo-generated current, and  $J_{dark}(V)$  is the dark current. We assume that the so-called “superposition principle” holds for the solar cell. The superposition principle can be assumed to be applicable to p–i–n junction solar cells whose mobility is high and to most of the p–n junction solar cells [16], [17]. The superposition principle states that the J–V characteristics of solar cells can be expressed using a voltage-independent photo-generated current and diode current under the dark condition. Thus, the following equations hold for p–n junction solar cells.

$$J_{ph}(V) = J_{SC} \quad (14)$$

$$\begin{aligned} J(V) &= J_{ph}(V) - J_{dark}(V) \\ &= J_{SC} - J_{em,0}(\exp(qV/kT) - 1) - J_{nr}(V) \\ &\approx J_{SC} - \frac{J_{em,0} \exp(qV/kT)}{\eta_{ext}(V)}. \end{aligned} \quad (15)$$

Based on the above-mentioned assumptions, we first calculated  $V_{OC}$  and then  $W_{OC}$  and  $W_{DB}$ .

$$\begin{aligned} J(V_{OC}) = 0 &= J_{SC} - \frac{J_{em,0} \exp(qV_{OC}/kT)}{\eta_{ext}(V_{OC})} \\ \therefore V_{OC} &= \frac{kT}{q} \ln \left( \eta_{ext}(V_{OC}) \frac{J_{SC}}{J_{em,0}} \right) \end{aligned} \quad (16)$$

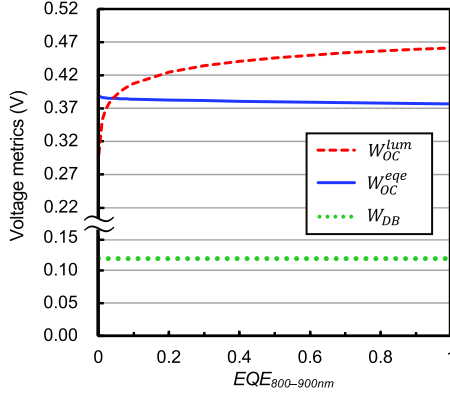


Fig. 2. Calculated values of  $W_{OC}^{lum}$ ,  $W_{OC}^{eqe}$ , and  $W_{DB}$ . These voltage metrics were calculated based on Assumptions 1–4.

$$\therefore W_{OC} = \frac{E_g}{q} - V_{OC} = \frac{E_g}{q} - \frac{kT}{q} \ln \left( \eta_{ext}(V_{OC}) \frac{J_{SC}}{J_{em,0}} \right) \quad (17)$$

$$\begin{aligned} W_{DB} &= V_{OC}^{DB} - V_{OC} = \frac{kT}{q} \ln \left( \frac{J_{SC}}{J_{em,0}} \right) - \frac{kT}{q} \\ &\quad \times \ln \left( \eta_{ext}(V_{OC}) \frac{J_{SC}}{J_{em,0}} \right) \\ &= -\frac{kT}{q} \ln(\eta_{ext}(V_{OC})). \end{aligned} \quad (18)$$

Equation (18) is well-known as the reciprocity relation proposed by Rau [15].  $W_{DB}$  described in [11] is the same metric described in Rau's article [15].

We calculated and plotted  $W_{OC}^{lum}$ ,  $W_{OC}^{eqe}$ , and  $W_{DB}$  as functions of the value of the EQE at 800–900 nm, as shown in Fig. 2. The temperature was assumed to be 25 °C.  $W_{OC}^{lum}$  is highly dependent on the EQE profiles and thickness of the active absorption layer, particularly when the EQE at the wavelength near the absorption edge is low, although  $\eta_{ext}(V_{OC})$  is constant, i.e., the nonradiative voltage loss is unchanged. Thus,  $W_{OC}^{lum}$  is not a suitable voltage metric to evaluate the nonradiative voltage losses among solar cells with different EQE profiles.

$W_{OC}^{eqe}$  is less dependent on the EQE at the wavelength near the absorption edge compared with  $W_{OC}^{lum}$ .  $W_{OC}^{eqe}$  can evaluate the radiative efficiency of the solar cells accurately if the effective bandgap does not differ a lot.  $W_{OC}^{eqe}$  changes by 10 mV, while the EQE at 800–900 nm changes from 0 to 1. This change is because of the dependence of  $W_{OC}^{eqe}$  on the bandgap. To observe this dependence, we assume the EQE to be expressed as follows:

$$EQE(\lambda) = \begin{cases} 1 & (300 \text{ nm} \leq \lambda \leq x \text{ [nm]}) \\ 0 & (\lambda \leq 300 \text{ nm}, \lambda \geq x \text{ [nm]}) \end{cases} \quad (19)$$

We calculated  $W_{OC}^{eqe}$  while changing the value of  $x$  from 400 to 1000 nm. The results are shown in Fig. 3.  $W_{OC}^{eqe}$  is strongly dependent on the value of  $x$ , which is determined by the bandgap. This dependence of  $W_{OC}$  on the bandgap was also reported for  $W_{OC}^{lum}$  [10]. Thus,  $W_{OC}^{eqe}$  is not a suitable metric for the accurate evaluation of the radiative efficiency of solar cells having largely different bandgaps.

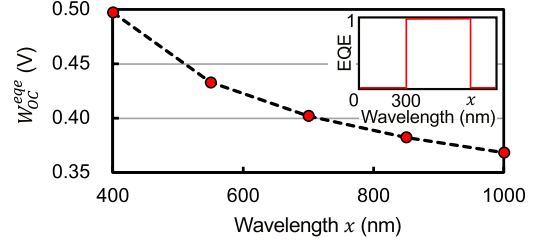


Fig. 3. Wavelength-dependent  $W_{OC}^{eqe}$  for the EQE profile defined in (19) and shown on upper right.

As (18) and Fig. 2 show,  $W_{DB}$  is only dependent on the ERE and is independent on the EQE profiles. Thus,  $W_{DB}$  is a suitable metric to compare the nonradiative voltage loss in solar cells, which have different EQE profiles.

### C. Voltage Metric for p-i-n Solar Cells

A quantum-structure is generally inserted into the i-region of p-i-n solar cells to realize efficient carrier transport. It is well-known that the original reciprocity relation [15] holds for most p-n junction solar cells but does not hold for p-i-n structure solar cells if the carrier mobility in i-region is quite low, e.g., 0.01 cm<sup>2</sup>/Vs [16], [17]. The superposition principle is the prerequisite for the original reciprocity relation, and it does not hold when the recombination process is nonlinear with regard to the carrier densities in solar cells. In the intrinsic region of p-i-n solar cells, the nonlinear Shockley–Read–Hall (SRH) process is the dominant recombination process. Thus, the original reciprocity relation, expressed in (18), does not hold for p-i-n solar cells if the carrier mobility is low and the SRH recombination is dominant in the entire solar cell.

It is known that the generalized reciprocity relation, (20), holds for p-i-n solar cells instead of the original one.

$$\begin{aligned} W_{DB} &= V_{OC}^{DB} - V_{OC} \\ &= -\frac{kT}{q} \ln(\eta_{ext}(V_{OC})) - \frac{kT}{q} \ln \left( \frac{F_c(V_{OC})}{F_i(V_{OC})} \right) \end{aligned} \quad (20)$$

where  $F_c(V_{OC})$  and  $F_i(V_{OC})$  are the spatial averages of local collection and local injection efficiencies, respectively [17], [18]. Except in some special cases,  $F_c(V)$  and  $F_i(V)$  can be written as follows:

$$F_c(V) = J_{ph}(V) / J_{phmax} \quad (21)$$

$$F_i(V) = \frac{1}{d} \int_0^d \frac{n(x, V) p(x, V) - n_i^2}{n_i \left[ \exp \left( \frac{qV}{kT} \right) - 1 \right]} dx \quad (22)$$

where  $J_{ph}(V)$  is photo-generated current in (13),  $J_{phmax}$  is the maximum photo-generated current,  $d$  is the thickness of the active layer,  $n(x, V)$  and  $p(x, V)$  are the electron and hole densities at position  $x$ , respectively, and  $n_i$  is intrinsic carrier density [18].

$W_{DB}$  is also dependent on  $F_c(V_{OC})$  and  $F_i(V_{OC})$ , which are determined by the mobility and solar cell structure. We experimentally examined whether the second term of  $W_{DB}$ ,



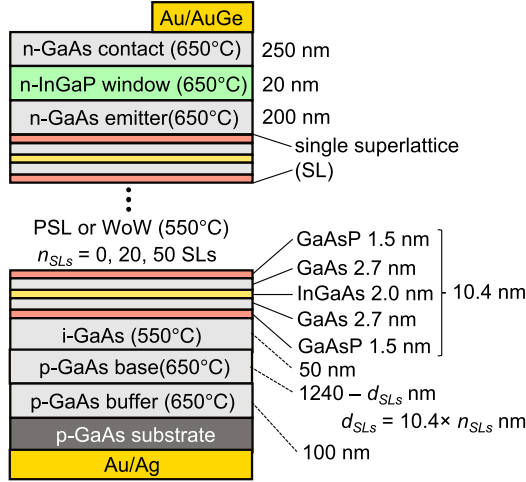


Fig. 4. Structure of the samples fabricated using MOVPE. Growth temperature of each layer is written within the brackets.

TABLE I  
LABELS OF SAMPLES AND THICKNESS OF SUPERLATTICE LAYERS

Labels	Structure	No. of layers, $n_{SLs}$	Thickness of SL layers, $d_{SLs}$ (nm)
GaAs ref.	GaAs bulk	-	0
20 PSL	PSL	20	208
50 PSL	PSL	50	520
20 WoW	WoW	20	208
50 WoW	WoW	50	520

GaAs ref. is a GaAs bulk solar cell treated as a reference sample.  $n_{SLs}$  and  $d_{SLs}$  are the parameters shown in Fig. 4.

$-\frac{kT}{q} \ln\left(\frac{F_c(V_{OC})}{F_i(V_{OC})}\right)$ , hinders the accurate estimation of the ERE of quantum-structure solar cells (cf. Table III).

### III. EXPERIMENTAL DETAILS

We fabricated p-i-n quantum-structure solar cells and performed EL measurements to prove that  $W_{DB}$  is a good voltage metric for evaluating the nonradiative voltage loss.

#### A. Sample Structures and Fabrication

p-i-n quantum-structure solar cell samples were grown using metal-organic vapor phase epitaxy (MOVPE) in a reactor AIX200/4 (AIXTRON). The main precursors used in the growth process were trimethylgallium (TMGa), trimethylindium (TMIn), tertiarybutylarsine (TBA), and tertiarybutylphosphine (TBP), and the doping precursors were dimethylzinc (DMZn) and hydrogen sulfide. The carrier gas was hydrogen, and the reactor pressure was 100 mbar. The structure of the sample is shown in Fig. 4. The quantum-structure was inserted into the i-layer of the p-i-n structure. Table I shows the labels of the samples shown in Fig. 4 and the number of layers of superlattices. The composition and thickness of the quantum-structure were determined using X-ray diffraction measurements. We prepared two types of quantum-structures, planar superlattice (PSL), and wire-on-well (WoW). PSL is a normal superlattice

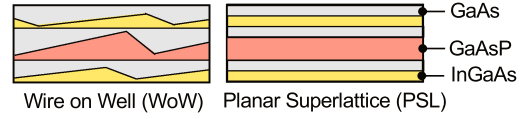


Fig. 5. Schematic cross-sectional image of each superlattice.

structure, which is obtained by growing a superlattice on a GaAs (0 0 1) substrate without misorientation. WoW is an undulated superlattice spontaneously obtained by growing the superlattice on a misoriented GaAs (0 0 1) substrate ( $6^\circ$  off toward  $\langle 1 \ 1 \ 1 \rangle_B$ ). Fig. 5 shows the schematic cross-sectional images of each superlattice. Cross-sectional scanning transmission electron microscope images of each superlattice are available in [19]. WoW has a locally thin-barrier region, which is expected to enhance the carrier tunneling probability. The characteristics of WoW are described in more detail in previous studies [19], [20].

For the GaAs reference sample (number of superlattices  $n_{SLs} = 0$ ), 50 nm-thick p-GaAs was grown instead of 50 nm-thick i-GaAs. The thickness of the p-GaAs base layer was adjusted to ensure the same total thickness of each sample while changing the number of superlattices (SLs)  $n_{SLs}$ . The samples with PSLs were grown on GaAs (0 0 1) 2-inch wafers without misorientation, and the samples with WoW were grown on  $6^\circ$ -off 2-inch wafers. For WoW, the thicknesses shown in this figure indicates the designed mean values that are susceptible to undulation. The doping concentration of the n-GaAs emitter and p-GaAs base was  $1 \times 10^{18} \text{ cm}^{-3}$  and  $3 \times 10^{17} \text{ cm}^{-3}$ , respectively. The superlattices and i-GaAs layer were not doped, and the estimated background doping concentration was  $10^{14} - 10^{15} \text{ cm}^{-3}$ . The quantum-structure layers were grown at  $550^\circ\text{C}$  because the WoW layers should be grown at a low temperature to suppress the lattice relaxation caused by step-bunching [21]. Unintentionally doped i-GaAs layers were also grown at  $550^\circ\text{C}$ . For the low temperature growth, triethylgallium (TEGa) was used as a source of Ga to suppress the background doping. It is well-known that TEGa decomposes well at low temperatures and prevents the incorporation of carbon impurities [22].

#### B. EL Measurement

The absolute EL measurement requires the calibration of complicated setups, as described in [23], [24], [25], and [26], which are time-consuming and costly [27]. In preceding studies, to perform approximately absolute EL measurements, the EL intensity was calibrated using the original optoelectronic reciprocity theorem [15] and EQE results [27], [28]. However, we could not assume that the original reciprocity theorem holds for quantum-structure solar cells; thereby, the calibration method proposed in the preceding studies could not be applied to quantum-structure solar cells in a strict manner.

Therefore, another calibration method was used to perform an approximately absolute luminescence measurement for quantum-structure solar cells. We calibrated the obtained EL measurement results using our setup with a standard Lambertian light source and the results corresponding to a standard GaAs single-junction solar cell sample. The EL measurement was performed on  $2 \times 2 \text{ mm}^2$  samples (the aperture area was

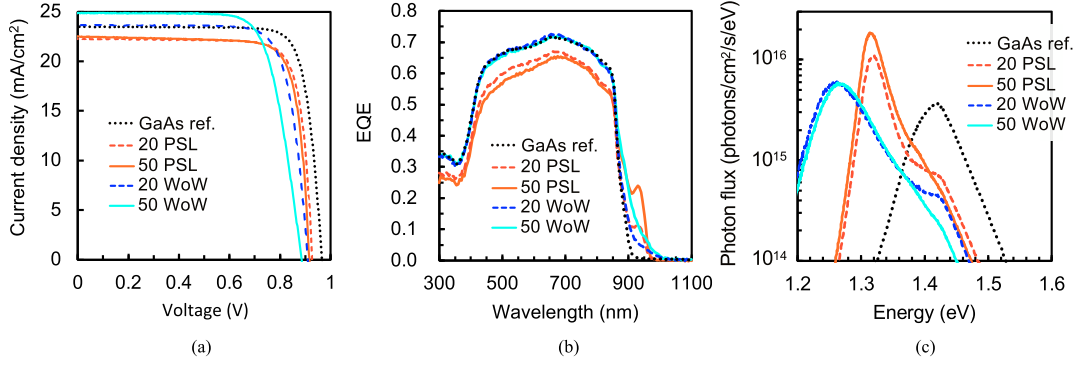


Fig. 6. (a) I–V characteristics under AM1.5. (b) EQE measurement results. (c) Absolute EL measurement results under room temperature, 25 °C. I–V characteristics are also summarized in Table I. For the EL measurement, the current injected into each sample was the short-circuit current density of itself.

3.01 mm<sup>2</sup>) by injecting a current equivalent to the short-circuit current at room temperature. The current was injected and kept constant using a sourcemeter (Keithley 2400). The field of view of our objective lens was about 500 μm in diameter. Therefore, the location-dependence of the EL intensity of our 2 × 2 mm<sup>2</sup> samples needs to be minor for accurate ERE measurements. A CCD camera (pco.1300, pco.) was used to confirm that the samples were uniformly emitting EL, and it was found that the EL intensity showed minor location-dependence (*cf.* Appendix B). The EL spectrum was measured using a spectrometer (Acton SP2300, Princeton Instruments). The wavelength-dependence of the sensitivity of the spectrometer was calibrated using a standard Lambertian light source (HL-3 plus-CAL, Ocean Optics) diffused using an integrating sphere (IS200, Thorlab). With this standard Lambertian light source, we obtained the calibration constant as follows:

$$C_{wave}(\lambda) = \frac{\phi_{HL-3}^{spec}(\lambda)}{\phi_{HL-3}^{ex}(\lambda)} \quad (23)$$

where  $\phi_{HL-3}^{spec}(\lambda)$  is the absolute photon flux spectrum written on the spec sheet, and  $\phi_{HL-3}^{ex}(\lambda)$  is the photon flux spectrum of the Lambertian light measured by our setup. We could not absolutely calibrate the EL spectrum emitted from a solar cell using  $C_{wave}$ , because, in our setup, we could not use the same light path for the standard Lambertian light source and EL emitted from a solar cell. Thus,  $C_{wave}$  was only used for the wavelength-dependence calibration of the sensitivity of the spectrometer. To obtain a calibration constant for absolute photon flux measurements, we used a standard GaAs single-junction solar-cell sample. The absolute photon flux emitted from this standard GaAs sample was measured in L’Institut Photovoltaïque d’Île-de-France (IPVF) using the setup described in [25]. We performed EL measurements for this standard sample using our setup and obtained the calibration constant for absolute EL measurements using the following equation:

$$C_{abs} = \frac{\Phi_{standard}^{abs}}{\int_0^\infty C_{wave}(\lambda) \phi_{jp}^{st}(\lambda) d\lambda} \quad (24)$$

where  $\Phi_{standard}^{abs}$  is the absolute photon flux emitted by the standard sample and measured using the special systems in France, and  $\phi_{jp}^{st}(\lambda)$  is EL spectrum emitted by the same standard

TABLE II  
I–V CHARACTERISTICS AND BANDGAP

Labels	$J_{sc}$ (mA/cm <sup>2</sup> )	$V_{oc}$ (V)	$FF$	$E_{g,lum}$ (eV)	$E_{g,0}$ (eV)	ERE, $\eta_{ext}$ (%)
GaAs ref.	23.47	0.966	0.814	1.420	1.408	0.239
20 PSL	22.20	0.927	0.813	1.319	1.352	0.466
50 PSL	22.50	0.916	0.803	1.316	1.334	0.737
20 WoW	23.65	0.910	0.779	1.261	1.332	0.462
50 WoW	24.87	0.886	0.736	1.268	1.315	0.368

$E_{g,lum}$  is the energy of the electroluminescence peak, as shown in Fig. 6(c).  $E_{g,0}$  was calculated from the EQE results presented in Fig. 6(b) and (7).

sample and measured using our setup in Japan. Finally, by using  $C_{wave}(\lambda)$  and  $C_{abs}$ , we calculated the absolute photon flux from the EL spectrum measured using our experimental setup

$$\Phi_{abs} = C_{abs} \int_0^\infty C_{wave}(\lambda) \phi_{raw}(\lambda) d\lambda \quad (25)$$

where  $\Phi_{abs}$  is the absolute EL flux, and  $\phi_{raw}(\lambda)$  is the raw EL spectrum measured using our setup. The ERE was calculated using  $\Phi_{abs}$  and (12).

#### IV. RESULTS AND DISCUSSION

Fig. 6 shows the results of the I–V, EQE, and EL measurements. The EQE values for the PSL samples over a range of 300–900 nm were lower than those for the WoW samples because of the poor carrier collection efficiencies [19], [20]. The bandgap ( $E_{g,lum}$ ) of each sample was determined using the EL peaks.  $E_{g,0}$  was calculated from the EQE results.  $E_{g,lum}$ ,  $E_{g,0}$ , and open-circuit voltages ( $V_{oc}$ ) of the samples are listed in Table II. The temperatures of the cells were roughly estimated from  $E_{g,lum}$ , and we assumed a temperature  $T = 303$  K. In our EL setup, we could not use a temperature-controlled sample stage for the absolute EL measurement, but we could use it for relative EL measurements. With our temperature-controlled sample stage, we could not accurately adjust the position of samples. However, we did not need the accurate sample position adjustment for measuring the EL peak energy  $E_{g,lum}$ . Thereby, we changed the temperature of the sample stage from 10 °C to 60 °C, and measured the EL peak energy, which was equal to

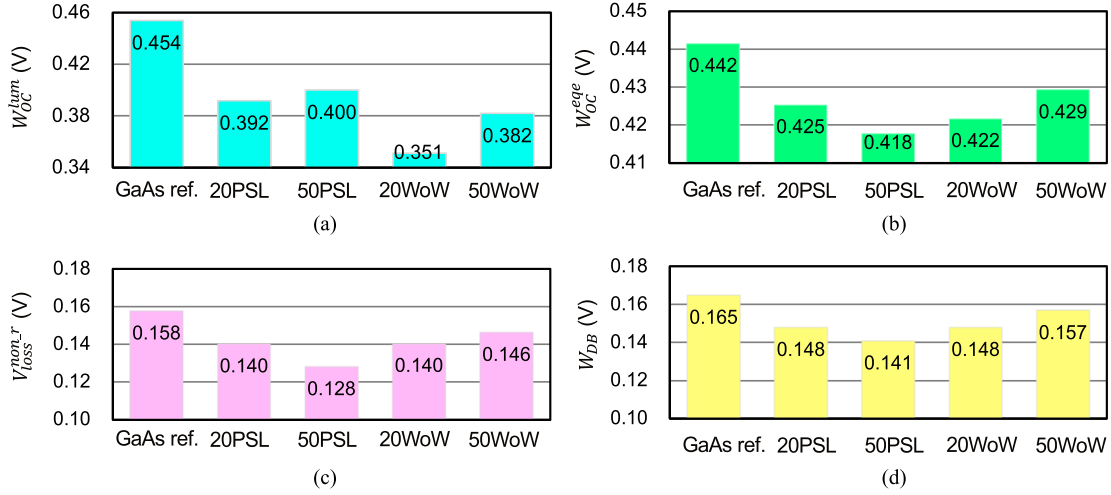


Fig. 7. Voltage metrics for the evaluation of the voltage loss in quantum-structure solar cells (a)  $W_{OC}^{lum}$ . (b)  $W_{OC}^{eqe}$ . (c)  $V_{loss}^{non-r}$ . (d)  $W_{DB}$ .

the value of  $E_{g,lum}$  shown in Table II, when the temperature of the sample stage was 30 °C (303 K).

$W_{OC}^{lum}$  was calculated using (1), and the results are shown in Fig. 7(a). Smaller values of  $W_{OC}^{lum}$  were achieved for the samples with fewer layers of superlattices. In samples with fewer layers of superlattices, the quasi-Fermi splitting was more significantly affected by the GaAs base layer. Thus, the samples with fewer layers of superlattices achieved a higher open-circuit voltage than those with more layers. By contrast, the bandgap ( $E_{g,lum}$ ) was not much affected by the number of superlattice layers. The luminescence peak is primarily determined using the effective band-edge of the superlattice, even if the total thickness of the superlattice layers is significantly smaller than that of the base material (GaAs). Therefore, the solar cell with fewer layers of superlattices achieved a smaller value of  $W_{OC}^{lum}$  than that with more layers. This tendency is in agreement with the theoretical calculation results shown in Fig. 2. Since  $W_{OC}^{lum}$  is significantly affected by the number of superlattice layers, it is not a suitable voltage metric for quantum-structure solar cells.

Next, we discuss the results of  $W_{OC}^{eqe}$ . The results are shown in Fig. 7(b).  $W_{OC}^{eqe}$  showed a varying tendency compared with that of  $W_{OC}^{lum}$ . Since the effective bandgap ( $E_{g,0}$ ) of each sample fabricated in the present study does not have a large difference, as shown in Table II,  $W_{OC}^{eqe}$  depends on the radiative efficiency rather than the bandgap. Therefore,  $W_{OC}^{eqe}$  showed similar tendency as that shown by  $V_{loss}^{non-r}$ , which is the voltage loss derived from the nonradiative recombination, as shown later in Fig. 7(c).

Here, we discuss the results of the ERE, calculated by integrating the EL spectrum shown in Fig. 6(c) using (12) and (25). The results are shown in Table II. The nonradiative voltage loss ( $V_{loss}^{non-r}$ ) was calculated using  $V_{loss}^{non-r} = -\frac{kT}{q} \ln(\eta_{ext}(V_{OC}))$ , and the results are shown in Fig. 7(c). The 50 PSL sample achieved the highest ERE, indicating the smallest nonradiative voltage loss. In PSL, carriers were strongly confined inside the quantum wells and recombined radiatively. This strong confinement of carriers resulted in lower carrier mobility in PSL compared with that in WoW [19], and carriers were stacked at small regions: quantum wells. The higher carrier density in quantum wells might be the reason of the higher ERE. The ERE

of the 50 WoW sample was smaller than that of the 20 WoW sample. This is because the 50 WoW sample has inferior crystal quality than that of the 20 WoW sample because of accumulated crystal strain. We designed and fabricated a strain-balanced quantum-structure, but it was not “perfectly” strain balanced. The composition and thickness conditioning should be more carefully conducted for WoW samples.

At last, we discuss the results of  $W_{DB}$ . Using (3) and (5),  $V_{OC}^{DB}$  was calculated using the EQE measurement results, as shown in Fig. 7(d). Comparing  $W_{DB}$  and voltage loss  $V_{loss}^{non-r}$  calculated using the ERE, it was found that they showed similar tendencies; for example, the 50 PSL sample achieved the smallest voltage loss, and the GaAs reference sample showed the largest voltage loss. Although the tendencies of  $W_{DB}$  and  $V_{loss}^{non-r}$  were similar, the absolute value of each parameter differed by 10 mV approximately. For example,

$$W_{DB}^{GaAs\ ref} - V_{loss, GaAs\ ref}^{non-r} = 7\text{ mV} \quad (26)$$

where  $W_{DB}^{GaAs\ ref}$  and  $V_{loss, GaAs\ ref}^{non-r}$  are  $W_{DB}$  and  $V_{loss}^{non-r}$  of the GaAs ref. sample, respectively. Here, we introduce the measurement error  $v_{err}^{mes}$ . Equation (26) can be rewritten and generalized as follows:

$$\begin{aligned} W_{DB} - V_{loss}^{non-r} &= -\frac{kT}{q} \ln(\eta_{ext}(V_{OC})) \\ &\quad - \frac{kT}{q} \ln\left(\frac{F_c(V_{OC})}{F_i(V_{OC})}\right) - (V_{OC}^{DB} - V_{OC}) + v_{err}^{mes} \\ &= \frac{kT}{q} \left\{ -\ln(\eta_{ext}(V_{OC})) - \ln\left(\frac{F_c(V_{OC})}{F_i(V_{OC})}\right) - \ln\left(\frac{J_{SC}}{J_{em,0}}\right) \right. \\ &\quad \left. + \ln\left(\eta_{ext}(V_{OC}) \frac{J_{SC}}{J_{em,0}}\right) \right\} \\ &\quad + v_{err}^{mes} = -\frac{kT}{q} \ln\left(\frac{F_c(V_{OC})}{F_i(V_{OC})}\right) + v_{err}^{mes}. \end{aligned} \quad (27)$$

The value of  $-\frac{kT}{q} \ln(F_c(V_{OC})/F_i(V_{OC}))$  of the GaAs ref. sample should be approximately zero as it does not have an i-region; as mentioned in Section III-A, 50 nm-thick p-GaAs

TABLE III  
MEASUREMENT ERROR AND THE EFFECT OF CARRIER COLLECTION  
EFFICIENCY AND INJECTION EFFICIENCY

Labels	$W_{DB} - V_{loss}^{non-r}$ (mV)
GaAs ref.	7
20 PSL	8
50 PSL	13
20 WoW	8
50 WoW	11

was grown instead of 50 nm-thick i-GaAs. Thus, we can assume that  $v_{err}^{mes}$  is approximately 7 mV. We will investigate the source and uncertainty of this measurement error in future research. The possible sources are the instability and aging degradation of the standard Lambertian light source and standard GaAs sample. The calculated values of  $W_{DB} - V_{loss}^{non-r}$  for other samples are summarized in Table III. From these values, we found that the term  $-\frac{kT}{q} \ln(\frac{F_c(V_{OC})}{F_i(V_{OC})})$  for different samples differs only by less than a few mV. This is because the carrier mobility in a quantum-structure is high. It has been theoretically revealed that the term  $-\frac{kT}{q} \ln(\frac{F_c(V_{OC})}{F_i(V_{OC})})$  creates a difference only when the carrier mobility is quite low, e.g.,  $0.01 \text{ cm}^2/\text{Vs}$  [16]. In our previous study [20], we measured the effective carrier mobility in both PSL and WoW and found that the mobility was 1–5  $\text{cm}^2/\text{Vs}$ . We have experimentally proved that  $-\frac{kT}{q} \ln(\frac{F_c(V_{OC})}{F_i(V_{OC})})$  created a minor difference in high-mobility quantum-structure solar cells. Therefore, we can roughly estimate the ERE of our samples from  $W_{DB}$  (cf. Appendix C).

From the above-mentioned discussion, we can evaluate the nonradiative voltage loss accurately enough using  $W_{DB}$ , even though the samples prepared in this study had a p-i-n structure. Thus, the performance of the samples can be easily and fairly evaluated using  $W_{DB}$ , which only needs conventional EQE measurements. As mentioned before, absolute EL measurements enabled us to evaluate the nonradiative voltage loss accurately but required a specially and precisely calibrated measurement system, which is not easily available. In terms of availability, the  $W_{DB}$  measurement is superior to the ERE measurement, which needs absolute EL measurements. We showed that the nonradiative voltage loss in quantum-structure solar cells can be evaluated with sufficient accuracy by either ERE or EQE measurements.

## V. CONCLUSION

In this article, we have compared the various voltage metrics used for evaluating the performance of solar cells to clarify and summarize the pros and cons of each metric used in the solar cell community. Each voltage metric was applied to solar cells with the careful consideration of avoiding misleading evaluations of the voltage loss. We have theoretically and experimentally proved that the nonradiative voltage loss in solar cells, including p-i-n quantum-structure solar cells, can be easily and accurately evaluated using  $W_{DB}$  measurements. Since the superposition rule does not hold for p-i-n junction solar cells, it was not clear whether  $W_{DB}$  is applicable to p-i-n junction solar cells.

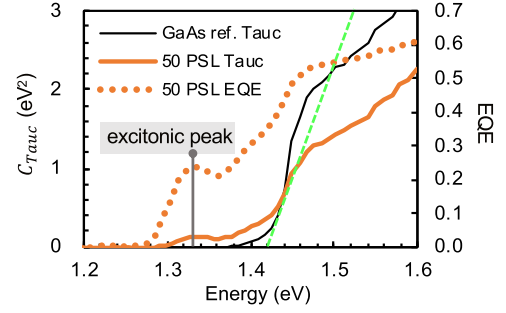


Fig. 8. Tauc plot of GaAs ref. and 50 PSL samples.

In p-i-n junction solar cells,  $W_{DB}$  was not only dependent on the nonradiative voltage loss but also dependent on carrier collection and carrier injection efficiencies. In this study, we have experimentally demonstrated that the carrier collection and injection efficiency factors can be ignored for p-i-n junction solar cells that have sufficiently high carrier mobility. Thus,  $W_{DB}$  measurements do not need special setups like absolute EL measurements because  $W_{DB}$  is calculated using conventional EQE measurements. The nonradiative voltage loss in solar cells that have different EQE profiles was accurately, fairly, and easily evaluated using  $W_{DB}$ ; this will facilitate the development of high-performance solar cell technology.

## APPENDIX

### A. Various Calculation Methods of the Bandgap of Solar Cells

There are various methods for calculating the effective bandgap of solar cells using the EQE. In this appendix, we introduce some of these methods, which we found not to be applicable to quantum-structure solar cells. Thus, we used only two types of effective bandgap, as indicated in Section II-A.

#### 1) Tauc plot method [29]

In this method, the Tauc plot written as follows:

$$C_{Tauc}(E) = [E \times \ln(1 - Q_e)]^2 \quad (28)$$

was used [29], [30], [31]. Fig. 8 shows  $C_{Tauc}(E)$  of the GaAs ref. and 50 PSL samples, and the EQE result of the 50 PSL sample. The intersection of the light-green dashed line and the horizontal axis is considered as the effective bandgap in this method. It appeared that the Tauc plot of the 50 PSL sample could be fitted with the light-green dashed line. However, the excitonic peak of the EQE of the 50 PSL sample was completely ignored as shown in Fig. 8 using the light-green dashed line. The excitonic peak of the EQE was over 20%; therefore, this part could not be ignored for the calculation of the effective bandgap. Compared with the Tauc plot of the GaAs ref. sample, the Tauc plot of the 50 PSL sample was more complicated. We could not figure out at which energy we had to fit and draw the light-green dashed line to accurately evaluate the effective bandgap of the 50 PSL sample.

#### 2) Semilogarithmic plot method [32]

This method was proposed by Helmer et al. In Fig. 9, we plotted the semilogarithmic EQE of the GaAs ref. and 50 PSL samples. In this method, the effective bandgap of each sample



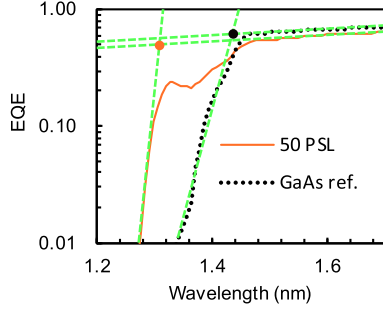


Fig. 9. Semilogarithmic EQE result.

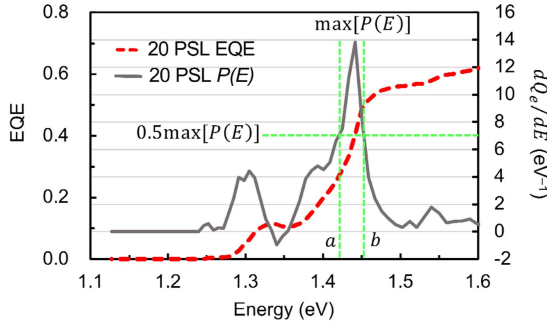


Fig. 10. Distribution function method proposed in [33].

was determined by the intersection point of two exponential fits as shown in Fig. 9. The detailed procedure is presented in [32]. The effective bandgap of the 50 PSL sample was determined only from the EQE tail of PSL and the contribution of the GaAs layer to the effective bandgap was completely ignored.

### 3) Distribution function method [33]

In this method,  $P(E) = dQ_e/dE$  was used as the distribution function, and the effective bandgap  $E_g^{PV}$  was calculated using the following equation:

$$E_g^{PV} = \int_a^b EP(E) dE / \int_a^b P(E) dE. \quad (29)$$

The energies  $a$  and  $b$  were chosen as the energy where  $P(E)$  was equal to  $0.5 \max[P(E)]$ , as shown in Fig. 10. We found that the effective bandgap of quantum-structure solar cells was determined only by the GaAs layers. We also found that the sigmoid function method [34] was not either suitable for quantum-structure solar cells, which have large excitonic peaks. This sigmoid function method used a similar procedure as this distribution function method.

## B. Location-Dependence of EL Intensity

We evaluated the location-dependence of the EL intensity. Fig. 11 shows, as an example, the EL image of the 20 PSL sample obtained by the CCD camera. To evaluate the location-dependence quantitatively, we performed line scan analysis, as shown in Fig. 11. We prepared eight lines in the horizontal direction (1)–(8) and four sections (a)–(d). In total,  $N = 8 \times 4 = 32$  sections were prepared. Each section had 68 pixels. The length of each section was  $500 \mu\text{m}$ , which was the same value as

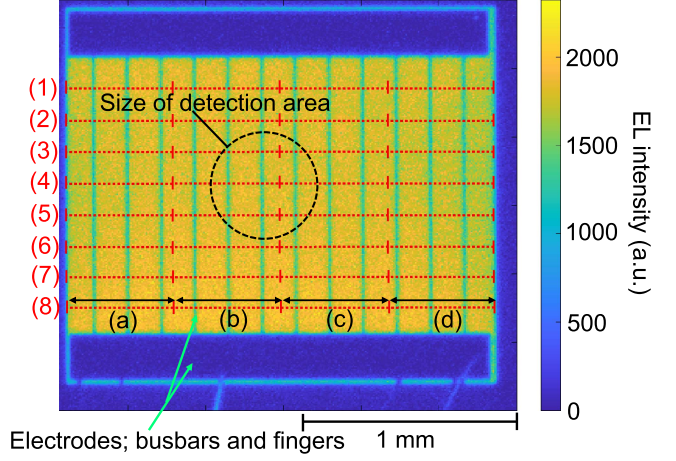


Fig. 11. EL image of the 20 PSL sample.

TABLE IV  
AVERAGES OF EL INTENSITY OF EACH SECTION

	(a)	(b)	(c)	(d)
(1)	1758	1787	1760	1693
(2)	1712	1767	1748	1669
(3)	1739	1773	1744	1652
(4)	1720	1763	1755	1645
(5)	1729	1771	1770	1676
(6)	1733	1803	1784	1700
(7)	1773	1820	1836	1753
(8)	1855	1860	1866	1792

the diameter of the detection area of the objective lens for the absolute EL measurement. Averages of EL intensity of each section were calculated. The results are shown in Table IV. The average of these 32 averages was  $\mu = 1756$ , and their standard deviation was  $\sigma = 55.6$ . All of the 32 averages were in the range of  $(1 \pm 0.063)\mu$ . This location-dependence makes little change in the open-circuit voltage,  $\frac{k_B T}{q} \ln 1.063 = 1.57 \text{ mV}$ .

## C. Estimation of ERE From $W_{DB}$

We estimated the ERE from  $W_{DB}$ . The quantum-structure solar cells presented in this study had high carrier mobility, so that we could assume that  $W_{DB} \approx V_{loss}^{non-r}$  and calculate the ERE using (18). Table V shows the ERE ( $\mu_{ext}^{EL}$  and  $\mu_{ext}^{W_{DB}}$ ) calculated from the EL results and  $W_{DB}$ . There were approximately 30% (0.3) errors.  $W_{DB}$  could be used for rough approximation of the ERE. Note that there was approximately 7 mV of measurement error  $v_{err}^{mes}$  in our setups. If we can eliminate this error, the ERE can be calculated more accurately as shown in Table VI. The errors would be less than 20%.

TABLE V  
ERE CALCULATED FROM  $W_{DB}$

Labels	$\mu_{ext}^{EL}$ (%)	$\mu_{ext}^{W_{DB}}$ (%)	$(\mu_{ext}^{EL} - \mu_{ext}^{W_{DB}})/\mu_{ext}^{EL}$
GaAs ref.	0.239	0.180	0.246
20 PSL	0.466	0.346	0.258
50 PSL	0.737	0.452	0.387
20 WoW	0.462	0.346	0.252
50 WoW	0.368	0.245	0.335

TABLE VI  
ERE CALCULATED FROM  $W_{DB}$  WITHOUT  $v_{err}^{mes}$

Labels	$\mu_{ext}^{W_{DB}}$ (%)	$(\mu_{ext}^{EL} - \mu_{ext}^{W_{DB}})/\mu_{ext}^{EL}$
GaAs ref.	0.236	0.014
20 PSL	0.452	0.030
50 PSL	0.591	0.199
20 WoW	0.452	0.022
50 WoW	0.320	0.131

#### ACKNOWLEDGMENT

The standard GaAs sample used for the calibration of the absolute EL measurement setup referred to in Section III-B was provided by L'Institut Photovoltaïque d'Île-de-France (IPVF). The authors would like to thank the members of IPVF, Prof. J. F. Guillemoles and Dr. A. Delamarrea.

#### REFERENCES

- [1] W. Shockley and W. T. Read, "Statistics of the recombinations of holes and electrons," *Phys. Rev.*, vol. 87, no. 5, pp. 835–842, 1952.
- [2] T. Nakamura et al., "Reducing Shockley–Read–Hall recombination losses in the depletion region of a solar cell by using a wide-gap emitter layer," *Appl. Phys.*, vol. 130, 2021, Art. no. 153102.
- [3] M. Yamaguchi et al., "Role of PV-powered vehicles in low-carbon society and some approaches of high-efficiency solar cell modules for cars," *Energy Power Eng.*, vol. 12, pp. 375–395, 2020.
- [4] R. R. King et al., "Band gap-voltage offset and energy production in next-generation multijunction solar cells," *Prog. Photovolt.: Res. Appl.*, vol. 19, pp. 797–812, 2011.
- [5] T. Aho et al., "Thin-film InAs/GaAs quantum dot solar cell with planar and pyramidal back reflectors," *Appl. Opt.*, vol. 59, pp. 6304–6308, 2020.
- [6] C. G. Bailey et al., "Improved bandgap-voltage offset in InGaAs/InAlGaAs quantum well solar cells," in *Proc. IEEE 39th Photovolt. Specialists Conf. PART 2*, 2013, pp. 032–037.
- [7] K. Toprasertpong et al., "Absorption threshold extended to 1.15 eV using InGaAs/GaAsP quantum wells for over-50%-efficient lattice-matched quad-junction solar cells," *Prog. Photovolt.: Res. Appl.*, vol. 24, pp. 533–542, 2016.
- [8] K. Shervin, W. Wang, K. Kharel, M. P. Fitchette, and A. Freundlich, "Graded superlattice and resonantly coupled quantum wells for dilute nitride solar cells with open circuit voltages that exceed that of the absorber's radiative limit," in *Proc. IEEE 7th World Conf. Photovolt. Energy Convers.*, 2018, pp. 2763–2766.
- [9] I. E. Hashem Sayed, C. Z. Carlin, B. G. Hagar, P. C. Colter, and S. M. Bedair, "Strain-balanced InGaAsP/GaInP multiple quantum well solar cells with a tunable bandgap (1.65–1.82 eV)," *IEEE J. Photovolt.*, vol. 6, no. 4, pp. 997–1003, Jul. 2016.
- [10] N. Ekins-Daukes and A. Pusch, "The use and abuse of  $W_{oc}$  as a figure of merit," in *Proc. 35th Eur. Photovolt. Sol. Energy Conf. Exhib.*, 2018, pp. 12–14, Paper 1AO.1.3.
- [11] E. S. Toberer, A. C. Tamboli, M. A. Steiner, and S. Kurtz, "Analysis of solar cell quality using voltage metrics," in *Proc. 38th IEEE Photovolt. Specialists Conf.*, 2012, pp. 001327–001331.
- [12] I. E. H. Sayed, N. Jain, M. A. Steiner, J. F. Geisz, and S. M. Bedair, "100-period InGaAsP/InGaP superlattice solar cell with sub-bandgap quantum efficiency approaching 80%," *Appl. Phys. Lett.*, vol. 111, 2017, Art. no. 082107.
- [13] J. F. Geisz et al., "Generalized optoelectronic model of series-connected multijunction solar cells," *IEEE J. Photovolt.*, vol. 5, no. 6, pp. 1827–1839, Nov. 2015.
- [14] M. A. Steiner et al., "Apparent bandgap shift in the internal quantum efficiency for solar cells with back reflectors," *J. Appl. Phys.*, vol. 121, 2017, Art. no. 164501.
- [15] U. Rau, "Reciprocity relation between photovoltaic quantum efficiency and electroluminescent emission of solar cells," *Phys. Rev. B*, vol. 76, 2007, Art. no. 085303.
- [16] T. Kirchartz and U. Rau, "Detailed balance and reciprocity in solar cells," *Phys. Statist. Sol. A*, vol. 205, 2008, Art. no. 2737.
- [17] K. Toprasertpong, A. Delamarrea, Y. Nakano, J. F. Guillemoles, and M. Sugiyama, "Generalized reciprocity relations in solar cells with voltage-dependent carrier collection: Application to p-i-n junction devices," *Phys. Rev. Appl.*, vol. 11, 2019, Art. no. 024029.
- [18] T. Kirchartz, J. Nelson, and U. Rau, "Reciprocity between charge injection and extraction and its influence on the interpretation of electroluminescence spectra in organic solar cells," *Phys. Rev. Appl.*, vol. 5, 2016, Art. no. 054003.
- [19] M. Sugiyama et al., "Quantum wire-on-well (WoW) cell with long carrier lifetime for efficient carrier transport," *Prog. Photovolt.: Res. Appl.*, vol. 24, pp. 1606–1614, 2016.
- [20] M. Asami et al., "Comparison of effective carrier mobility between wire on well and planar superlattice using time-of-flight measurement," *IEEE J. Photovolt.*, vol. 10, no. 4, pp. 1008–1014, Jul. 2020.
- [21] H. Fujii et al., "Thickness modulated InGaAs/GaAsP superlattice solar cells on vicinal substrates," *J. Appl. Phys.*, vol. 117, 2015, Art. no. 154501.
- [22] H. Fujii et al., "InGaAs/GaAsP superlattice solar cells with reduced carbon impurity grown by low-temperature metal-organic vapor phase epitaxy using triethylgallium," *J. Appl. Phys.*, vol. 116, pp. 203101–1–203101–8, 2014.
- [23] M. Yoshita et al., "Accuracy evaluations for standardization of multi-junction solar-cell characterizations via absolute electroluminescence," in *Proc. IEEE 43rd Photovolt. Specialists Conf.*, 2016, pp. 3570–3573.
- [24] T. Mochizuki et al., "Solar-cell radiance standard for absolute electroluminescence measurements and open-circuit voltage mapping of silicon solar modules," *J. Appl. Phys.*, vol. 119, 2016, Art. no. 034501.
- [25] A. Delamarrea, L. Lombez, and J. F. Guillemoles, "Contactless mapping of saturation currents of solar cells by photoluminescence," *Appl. Phys. Lett.*, vol. 100, 2012, Art. no. 131108.
- [26] A. Delamarrea et al., "Investigation of solar cell properties by absolute measurement of spatially and spectrally resolved luminescence," in *Proc. 27th Eur. PV Sol. Energy Conf. Exhib.*, 2012, pp. 497–499.
- [27] K. Toprasertpong et al., "Electroluminescence-based quality characterization of quantum wells for solar cell applications," *J. Cryst. Growth*, vol. 464, pp. 94–99, 2017.
- [28] T. Inoue et al., "Quasi-Fermi level splitting evaluation based on electroluminescence analysis in multiple quantum-well solar cells for investigating cell performance under concentrated light," *Proc. SPIE*, vol. 9743, 2016, Art. no. 974316.
- [29] J. Tauc, "Optical properties and electronic structure of amorphous Ge and Si," *Mater. Res. Bull.*, vol. 3, pp. 37–46, 1968.
- [30] R. Carron et al., "Bandgap of thin film solar cell absorbers: A comparison of various determination methods," *Thin Solid Films*, vol. 669, pp. 482–486, 2019.
- [31] B. G. Mendis et al., "Nanometre-scale optical property fluctuations in  $\text{Cu}_2\text{ZnSnS}_4$  revealed by low temperature cathodoluminescence," *Sol. Energy Mater. Sol. Cells*, vol. 174, pp. 65–76, 2018.
- [32] H. Helmers, C. Karcher, and A. W. Bett, "Bandgap determination based on electrical quantum efficiency," *Appl. Phys. Lett.*, vol. 103, 2013, Art. no. 032108.
- [33] U. Rau, B. Blank, T. C. M. Müller, and T. Kirchartz, "Efficiency potential of photovoltaic materials and devices unveiled by detailed-balance analysis," *Phys. Rev. Appl.*, vol. 7, 2017, Art. no. 044016.
- [34] O. Almora et al., "Quantifying the absorption onset in the quantum efficiency of emerging photovoltaic devices," *Adv. Energy Mater.*, vol. 11, 2021, Art. no. 2100022.